



UNIVERSITY OF LEEDS

This is a repository copy of *Fundamental studies of carbon capture using CaO-based materials*.

White Rose Research Online URL for this paper:
<http://eprints.whiterose.ac.uk/146218/>

Version: Accepted Version

Article:

Sun, H, Wang, J, Liu, X et al. (6 more authors) (2019) Fundamental studies of carbon capture using CaO-based materials. *Journal of Materials Chemistry A*, 7 (16). pp. 9977-9987. ISSN 2050-7488

<https://doi.org/10.1039/c8ta10472g>

© The Royal Society of Chemistry 2019. This is an author produced version of a paper published in *Journal of Materials Chemistry A*. Uploaded in accordance with the publisher's self-archiving policy.

Reuse

Items deposited in White Rose Research Online are protected by copyright, with all rights reserved unless indicated otherwise. They may be downloaded and/or printed for private study, or other acts as permitted by national copyright laws. The publisher or other rights holders may allow further reproduction and re-use of the full text version. This is indicated by the licence information on the White Rose Research Online record for the item.

Takedown

If you consider content in White Rose Research Online to be in breach of UK law, please notify us by emailing eprints@whiterose.ac.uk including the URL of the record and the reason for the withdrawal request.



eprints@whiterose.ac.uk
<https://eprints.whiterose.ac.uk/>

Fundamental studies of carbon capture using CaO-based materials

Hongman Sun,^{ab} Jianqiao Wang,^c Xiaotong Liu,^b Boxiong Shen,^{*c} Christopher M. A. Parlett,^{*d} George O. Adwek,^c
Edward J. Anthony,^{*e} Paul T. Williams^{*f} and Chunfei Wu^{*abc}

^a School of Chemistry and Chemical Engineering, Queen's University Belfast, Belfast BT7 1NN, UK

^b School of Engineering and Computer Science, University of Hull, Hull HU6 7RX, UK

^c School of Energy and Environmental Engineering, Hebei University of Technology, Tianjin 300401, China

^d School of Chemical Engineering and Analytical Science, University of Manchester, Manchester M1 3AL, UK

^e Centre for Combustion and CCS, Cranfield University, Cranfield MK43 0AL, UK

^f School of Chemical and Process Engineering, University of Leeds, Leeds LS2 9JT, UK

Abstract: Detailed understanding of the mechanisms of the fast stage during CaO carbonation is important to the design of novel efficient CaO materials. This work systematically studies the formation of CaCO₃ product layer on the outside surface of CaO grains during the fast reaction stage for carbon capture using two types of CaO adsorbents. The carbonation at 400 °C filled the small pores in the commercial CaO grains and no distinct product layer of CaCO₃ was observed. However, a distinct layer of CaCO₃ with a thickness around 90 nm was observed on the outside surface of the commercial CaO grains after the carbonation at 600 °C because the internal pores in the CaO grain had been filled and a layer of CaCO₃ product was deposited on the outside surface of the CaO grain. For sol-gel CaO, the carbonation reaction is limited by the availability of useful porosity for the growth of CaCO₃ product (confinement effect), instead of by the diffusion of ions in the critical layer of the CaCO₃ product. No surface product layer was observed. Therefore, fabricating nano-CaO having dimensions less than the critical thickness of the CaCO₃ layer (~90 nm) is of potentially great significance if it can be done cheaply and in bulk.

*Corresponding authors:

E-mail: c.wu@qub.ac.uk (C. Wu); p.t.williams@leeds.ac.uk (P.T. Williams), b.j.anthony@cranfield.ac.uk (E.J. Anthony); christopher.parlett@manchester.ac.uk (C. Parlett); shenbx@hebut.edu.cn (B. Shen).

24 **1. Introduction**

25 Greenhouse gas especially CO₂ emissions are responsible for climate change and the reduction of
26 greenhouse gas is important to the sustainable development of modern society.¹ It has been reported
27 by the Intergovernmental Panel on Climate Change (IPCC) that the global risks of climate change are
28 increasingly clear for agriculture, human health, ecosystems, and water supplies. The IPCC concluded
29 in 2014 that the world was ill-prepared for such risks.² Subsequently, the Parties to the United Nations
30 Framework Convention on Climate Change (UNFCCC) reached a landmark agreement (the Paris
31 Agreement) to accelerate actions and increase investments towards a sustainable and low-carbon
32 future.³ Carbon capture and utilisation (CCU) have been attracting increasing attention.^{4, 5} CO₂
33 absorption using amine solution is commercially available. However, as noted by Haszeldine et al.⁶
34 and Sadiq et al.,⁷ an estimated 30% of power plant output is required for the regeneration of sorbents
35 for carbon capture from post-combustion flue gas, because heating water in the amine sorbent causes
36 large energy losses. On the other hand, using solid sorbents to capture CO₂ is attractive, with the
37 following advantages: (1) the lower heat capacity of solids significantly reduces the sensible energy
38 required for sorbent regeneration; (2) corrosion problems caused by the use of amine solutions (the
39 current standard carbon capture method) are avoided;⁸ (3) heat released during the exothermic carbon
40 capture reaction at a high operating temperature (comparable to gas turbine exhaust temperature)⁹ can
41 be extracted by steam for power generation enabling a highly efficient steam cycle. CaO, as one of
42 the high-temperature CO₂ sorbents, has been investigated extensively because of its high reactivity
43 for CO₂ capture and high theoretical uptake capacity of 17.8 mmol g⁻¹, as well as the extensive
44 availability of CaO precursors possessing a low-cost nature.¹⁰⁻¹⁴ One 1 MWth long-term pilot testing
45 facility and a 1.7 MWth CaL pilot were constructed in Technische Universität Darmstadt and La
46 Pereda power plant, respectively.^{15, 16} It was found that the semi-industrial CaL plants achieved an

47 outstanding CO₂ capture efficiency (>90%) with a good operation stability (1200 h). In addition, a
48 1.9 MWth pilot plant constructed at 2013 in Taiwan confirmed that the CaL process is a promising
49 technology for CO₂ capture.¹⁷ However, one of the main limitations of CaO derived from natural
50 precursors is the sorbent deactivation during the regeneration process due to the sintering of CaO
51 particles at high regeneration temperature.¹⁸⁻²⁰ This behaviour can be explained by considering the
52 dramatic volume change between CaO and CaO to CaCO₃; for example an increase from 16.7 to 36.9
53 cm³ mol⁻¹ for CaO to CaCO₃. Furthermore, there are two stages in the carbonation reaction of CaO:
54 an initially fast reaction stage and a subsequently slow reaction stage.²¹⁻²³ It is attributed that the
55 reduction of carbonation rate in the slow stage was caused by the CO₂ diffusion through the formed
56 CaCO₃ product.²² In the carbonation process, the ratio of reaction rates between the fast and slow
57 reaction stages was around 100.²⁴ This value is in good consistency with the ratio of diffusion
58 coefficients for CaO (0.3 cm² s⁻¹) and CaCO₃ (0.003 cm² s⁻¹).^{22, 25} Therefore, Barker suggested that
59 there was a critical CaCO₃ product layer at which the carbonation reaction rate was determined by
60 the CO₂ diffusion.²² During the fast reaction stage, CaCO₃ grew on the surface of CaO grains and
61 then collapsed to form a continuous layer on the outside surface of the unreacted adsorbent. Thereafter,
62 the fast reaction stage during the CaO carbonation suddenly finished.²⁶ Thus, the initially fast stage
63 and the subsequently slow stage were controlled by the kinetic reaction and CO₂ diffusion through
64 the CaCO₃ product layer, respectively.^{27, 28}

65 To better understand the fast stage during the CaO carbonation, which is particularly essential for
66 practical applications due to the short reaction time, the critical thickness of the CaCO₃ product layer
67 has been extensively studied. Barker²² demonstrated a “critical carbonate layer thickness” of 22 nm
68 at which the carbonation reaction rate started to be controlled by CO₂ diffusion limitation. However,
69 the estimating equation adopted in that research was confounded by the uncertainties in the

70 carbonation model. A better understanding of pore model coupled with a carbonation pattern across
71 CaO particles was required in this model. In order to eliminate the influences of the unquantifiable
72 and complex morphology in natural materials, the long-duration carbonation reaction on non-porous
73 CaO particles was carried out by Mess et al.²⁹ It was found that the CaCO₃ product layer was
74 homogeneous and exhibited a thickness up to 2 μm under very severe carbonation conditions (850 °C
75 and 1.2 MPa of CO₂ for 2000 min). Subsequently, Alvarez and Abanades³⁰ refined the model
76 proposed by Barker²² and suggested that before the maximum product thickness was reached, the
77 small pores in the sorbent were completely filled. In their proposed model, a CaCO₃ layer was
78 generated on the outside surface of CaO grains in the carbonation reaction and an average value of
79 49 nm (standard deviation is around 19%) was determined.

80 However, the critical thickness of the CaCO₃ layer has only been estimated by means of computer-
81 aided modeling.^{22, 26, 29, 30} There has been no direct observation and measurement of the critical
82 thickness of CaCO₃ product layer formed in the CaO carbonation reaction. Thus, a detailed
83 experimental study is highly desirable for the design of novel CaO adsorbents and the understanding
84 of mechanisms of CaO carbonation.

85 In addition, most of the CaO carbonation work in the open literature was carried out at temperatures
86 higher than 500 °C. Only limited information on low-temperature carbonation of CaO at around 400
87 °C has been reported due to the relatively low reaction rate and low capacity of carbon capture.^{31, 32}

88 We have found that there are two stages of fast CaO carbonation maximising the reaction rate at 400
89 and 600 °C, respectively. Normally, one stage of the fast carbonation reaction was reported in other
90 work for non-isothermal CaO carbonation when the temperature was increased from room
91 temperature to 900 °C.³³ However, the presence of the carbonation gap between 400 and 600 °C has
92 not been clearly understood.

93 Furthermore, a potentially novel intensified process combining CO₂ capture and utilisation at around
94 400 °C could be very interesting. For example, Duyar et al.³⁴ reported that using a dual-functional
95 catalyst for CO₂ capture at 320 °C, followed by the introduction of H₂ at the same reaction temperature,
96 resulted in the regeneration of sorbent and the production of methane. In this scenario, the
97 regeneration of sorbents and the conversion of captured CO₂ were processed without an energy-
98 intensive thermal-swing process. Therefore, it is of interest to understand the formation of the CaCO₃
99 layer during CaO carbonation at key reaction temperatures of 400 °C and 600 °C. In this work, two
100 types of CaO adsorbents possessing different porosities were studied in relation to the critical
101 thickness of CaCO₃ product layer.

102

103 **2. Experimental section**

104 **2.1 Adsorbent preparation**

105 A standard sol-gel process proposed by Santos et al.³⁵ was used to synthesise a CaO adsorbent.
106 Predetermined amounts of calcium nitrate tetrahydrate (Ca(NO₃)₂·4H₂O, Sigma-Aldrich, 99.99%)
107 and citric acid monohydrate (C₆H₈O₇·H₂O, Sigma-Aldrich, 99.99%) acting as chelation agent, were
108 added to the distilled water at room temperature (water and citric acid to metal ion molar ratios were
109 40:1 and 1:1, respectively). The mixture was continuously stirred at 80 °C to form a translucent pale-
110 yellow sol with good dispersion. After drying overnight at 130 °C of the prepared sol, the translucent
111 pale-yellow sol turned into a low-density foam. The obtained foam was then calcined in a muffle
112 furnace at 850 °C for 5 h with a heating rate of 2 °C min⁻¹. This synthesized sample was designated
113 as sol-gel CaO. A commercial CaO (Sigma-Aldrich, 99.99%) was used as the reference adsorbent
114 after dried overnight at 130 °C.

115 **2.2 Carbonation/calcination tests**

116 The carbon capture performance of adsorbents was conducted in both a fixed-bed reactor (as shown
117 in Fig. 1) and a thermogravimetric analyser (TGA, SDT Q600). In the case of the fixed-bed test, 500
118 mg of adsorbent was loaded into the sample tube (6.35 mm in diameter). Both the carbonation and
119 calcination processes were performed with a temperature-swing process with a heating rate of 10 °C
120 min⁻¹ under 15% CO₂ balanced with N₂. The total flow rate of gases was controlled at 100 mL min⁻¹.
121 The reacted CaO samples produced at both 400 °C and 600 °C in the fixed-bed reactor were denoted
122 as sol-gel FB-400 and sol-gel FB-600 for the sol-gel CaO, and FB-400 and FB-600 for the commercial
123 CaO, respectively. After calcination, the sample was denoted as FB-des. The same
124 carbonation/calcination test was repeated over 3 cycles.
125 During the TGA test, around 15 mg of adsorbent was placed in an alumina crucible and heated to 800
126 °C with a heating rate of 20 °C min⁻¹ under the N₂ atmosphere (100 mL min⁻¹). When the temperature
127 decreased to room temperature, further increasing the temperature to 400 °C, 15% CO₂ was used to
128 carbonate the sample for 10 h and then increase the temperature to 600 °C for 30 min.

129 The carbonation conversion was calculated as follows:³⁶

$$130 \quad X(\%) = \frac{m_t - m_0}{m_0} \cdot \frac{M_{\text{CaO}}}{M_{\text{CO}_2}} \cdot 100\% \quad (1)$$

131 where X is the carbonation conversion, m₀ is the mass of the sample after calcination, m_t is the mass
132 of the sample after carbonation for t minutes, and M_{CaO} and M_{CO₂} are the mole masses of CaO and
133 CO₂, respectively.

134 2.3 Characterisation of adsorbents

135 Powder X-ray diffraction (XRD) was performed on a PANalytical empyrean series 2 diffractometer
136 with Cu K α radiation. Data were analysed by X'pert Highscore plus software. N₂ adsorption-
137 desorption isotherms were collected using an ASAP 2000 analyser at -196 °C. The Brunauer-Emmett-
138 Teller (BET) surface area was calculated using the adsorption branch data at the relative pressure

139 (P/P₀) from 0.06 to 0.2, and the micropore volume (V_{micro}) was calculated by the t-plot method.³⁷ The
140 pore size distribution was calculated by the Barrett-Joyner-Halenda (BJH) method using nitrogen
141 desorption branch data.

142 The surface morphology and microstructure of samples were characterised using scanning electron
143 microscopy (SEM, a Stereoscan 360) and transmission electron microscopy (TEM, JEOL 2010),
144 respectively. For TEM analysis of bulky solid samples, the samples were ground, dispersed with
145 acetone, and then deposited on a Cu grid covered with a perforated carbon membrane.

146 A Nanolab Dualbeam focused ion beam (FIB)-SEM coupled with an energy-dispersive X-ray
147 spectroscopy (EDX) and TEM coupled with selected area electron diffraction patterns, were used to
148 characterise and examine the critical thickness of the product layer deposited on the carbonated
149 adsorbents. For FIB-SEM analysis, the samples were cut using a focused ion beam to produce small
150 cross-section samples, which were attached to TEM grids using a platinum binder. After that, the
151 grids with the cross-section samples were analysed using TEM.

152 The crystalline phase change during the carbonation process for CaO and sol-gel CaO was detected
153 by the in-situ XRD. The Bruker D8 Advance XRD equipped with an Anton-Paar XRK-900 high-
154 pressure XRD cell and a Cu α source (0.154 nm) was conducted to collect the XRD patterns. Sample
155 activation was conducted at 800 °C in pure N₂ (1 bar, 50 mL min⁻¹) for 60 min, with a heating rate of
156 10 °C min⁻¹ before cooling to 400 °C for data collection. The sample was pre-treated with 15% CO₂
157 balanced with N₂ for 60 min and XRD patterns were continuously collected with the scanning ranging
158 from 22.5° to 40° with a step size of 0.1° and dwell time of 1 s (15 min scans yielding 4 patterns to
159 observe the phase changes).

160

161 **3. Results and discussion**

162 **3.1 Characterisations of adsorbents**

163 N₂ adsorption-desorption isotherms and pore size distributions were conducted to determine the
164 structure of the CaO materials (Fig. 2). The textural properties of different CaO adsorbents are
165 summarised in Table 1. The BET surface area (38.51 m² g⁻¹) and total pore volume (0.1527 cm³ g⁻¹)
166 of the sol-gel CaO are much higher than those of the commercial CaO (20.96 m² g⁻¹ and 0.0314 cm³
167 g⁻¹, respectively) due to the presence of micro-scale agglomerates generated by the voids between the
168 nano-scale grains,³⁵ which favor CO₂ carbonation performance.^{38, 39} The BJH pore size distribution
169 (Fig. 2b) indicates the formation of abundant mesopores and macropores ranging from 2 to 100 nm
170 in the sol-gel CaO. The morphologies of the commercial CaO and the sol-gel CaO are displayed in
171 Fig. 3a and b, respectively. The commercial CaO possesses a compact structure with a smooth surface
172 and the diameter of CaO grains ranges from 1.5 to 2 μm (Fig. S1a). Compared to the commercial
173 CaO, the sol-gel CaO exhibits a much more fluffy and porous structure. In addition, the diameter of
174 the sol-gel CaO grains ranges from 120 nm to 180 nm as shown in Fig. S1b. Pores less than 10 nm
175 are observed in the commercial CaO as shown in Fig. 3g in agreement with the distribution of small
176 pores ranging from 2 nm to 10 nm in Fig. 2b. However, mesopores composed of nano-sized grains
177 are observed only in the sol-gel CaO, which is consistent with the BJH size distribution (Fig. 2b).

178 **3.2 Carbon capture testing**

179 The carbonation of CaO at 400 and 600 °C was observed using a fixed-bed reactor. As shown in Fig.
180 4a and b, both the commercial CaO and the sol-gel CaO exhibited a dramatic CaO conversion at 400
181 °C. However, a further increase in temperature resulted in a sudden reduction of carbonation rate at
182 around 500 °C for both samples. The carbonation rate of the CaO increased again when the
183 temperature reached 600 °C. However, as shown in Table 2, the CO₂ uptake, from the 1st cycle to the

184 2nd cycle, declined dramatically at a carbonation temperature of around 400 °C for both the
185 commercial CaO and the sol-gel CaO, while only a slight decrease of CO₂ uptake is observed after
186 carbonation at 600 °C. Compared to the 2nd cycle performance of CO₂ capture, the 3rd cycle carbon
187 capture exhibited slightly decreased carbonation rates at both 400°C and 600 °C. It is noted that all
188 characterizations of materials are from 1st cycle carbon capture. It is suggested that with the increase
189 of carbonation/calcination cycles, less effect was observed on the carbon capture performance at the
190 second carbonation stage at around 600 °C. A more detailed understanding of mechanisms in relation
191 to the increase of carbonation/calcination cycles is suggested for future.

192 In order to eliminate the influence of moisture and other impurities inside the sorbent, both the
193 commercial CaO and the sol-gel CaO samples were heated to 800 °C under N₂ atmosphere; then the
194 samples were cooled to 400 °C for the CO₂ capture stage. Fig. S2 shows that the weight of the CaO
195 sample was increased initially due to the carbonation reaction and then showed relative stability at
196 400 °C, indicating that carbonation of CaO was almost completed at 400 °C. In addition, the sample
197 was held at 400 °C for 10 h prior to heating it to 600 °C for further carbonation. This is to ensure that
198 CaO carbonation at 600 °C was not due to incomplete carbonation at 400 °C. As shown in Fig. S2,
199 carbonation is clearly observed at 600 °C indicating the presence of a true two-stage fast carbonation
200 of CaO at around 400 and 600 °C, respectively.

201 A few studies have reported the existence of a reaction rate gap in the CaO carbonation when the
202 temperature ranges from 400 to 600 °C. Bhatia and Perlmutter⁴⁰ proposed that when the temperature
203 was lower than 515 °C, the CaO carbonation reaction as shown in Eq. (2) and (3) took place on the
204 pore surface and was governed by the diffusion of CO₂ molecules with an activation energy of 88.9
205 ± 3.7 kJ mol⁻¹. The ionic diffusion process is shown in Fig. S3a. This is consistent with the
206 observation of CaO carbonation at around 400 °C in this work. However, increasing the temperature

207 of CaO carbonation to higher than 515 °C, the reaction was reported to take place at the interface
208 between CaO and CaCO₃ as described in Eq. (4), where CO₃²⁻ is the diffusion species with an
209 activation energy about 179.2 ± 7.0 kJ mol⁻¹ ⁴⁰ as shown in Fig. S3b.

210 T < 515 °C, carbonation occurs at the pore surface:



213 T > 515 °C, carbonation occurs at the CaO-CaCO₃ interface:



215 3.3 Mechanisms of CaO carbonation

216 XRD results for the CaO samples are shown in Fig. 5. For the fresh commercial CaO and sol-gel CaO
217 samples, only one CaO phase is observed. After carbonation at 400 °C, the spent adsorbents exhibit
218 a weak diffraction peak at 2θ = 29.4°, indicating the characteristic peak of CaCO₃ (1 0 4).⁴¹ The XRD
219 patterns for the commercial CaO and the sol-gel CaO after carbonation at 600 °C exhibit much
220 stronger diffraction peaks at similar positions. This indicates that more CaCO₃ phases were generated
221 at 600 °C compared with the reacted CaO sorbents obtained at 400 °C. The diffraction peaks of CaCO₃
222 disappear after increasing the carbonation temperature to 800 °C. This is attributed to the
223 decomposition of CaCO₃ at 800 °C.

224 After carbonation of the commercial CaO and the sol-gel CaO at 400 and 600 °C, similar
225 morphologies are observed for both FB-400 and FB-600 (Fig. 3c and e). From Fig. 3d and f, the
226 mesopores in the sol-gel CaO appear to diminish after carbonation at 400 and 600 °C. Nevertheless,
227 there are many attachments on the surface of the sol-gel CaO carbonated at 400 °C observed in the
228 SEM images (Fig. 3d), showing that the mesopores between small grains are well connected.
229 However, the sol-gel CaO experienced a dramatic decrease of pores and the growth of grains after

230 carbonation at 600 °C due to the volume increase of the sorbent, as shown in Fig. 3f.

231 FIB-SEM coupled with EDX was used to measure the critical thickness of the CaCO₃ product layer
232 as shown in Fig. 6. It is noted that the top layer observed in the cross-section was coated with indium
233 which was used to protect the surface during the cutting of the CaO samples.⁴² As for the commercial
234 CaO, no product layer can be observed after carbonation at 400 °C as shown in Fig. 6a. However, a
235 uniform distribution of carbon element is shown in EDX mapping (Fig. S4) implying that CaCO₃ was
236 formed uniformly within the commercial CaO during carbonation at 400 °C. The existence of CaCO₃
237 is also confirmed from the XRD analysis of FB-400 (Fig. 5a). The commercial CaO sample has a
238 bulk particle size around 3 mm with small grains (around 1.5 μm) containing small pores ranging
239 from 2 nm to 10 nm.^{43, 44} It appears that carbonation of the commercial CaO at 400 °C is dominated
240 by the kinetic reaction between CaO and CO₂, and the small pores in the grains were filled with the
241 CaCO₃ formed. Although a layer of CaCO₃ is not observed on the FB-400 sample, EDX analysis (Fig.
242 7a and b) shows that the concentration of carbon in relation to CaCO₃ inside the small grains of the
243 commercial CaO was around 5.44%, which is lower than the concentration of carbon on the surface
244 of the commercial CaO (6.16%) (FB-400). This indicates that the outer layer of the CaO was
245 concentrated with CaCO₃ in the fast carbonation stage at 400 °C.

246 A distinct layer is observed after the CaO sample was carbonated at 600 °C. It is suggested that after
247 the carbonation, the internal pores in the grain have been filled and a layer of product was formed on
248 the outside of the grain. It can be seen from Fig. S5 that the average thickness of the product (CaCO₃)
249 is around 90 nm. It is noted that the FB-600 sample was obtained when the maximum carbonation
250 rate was reached during carbonation at 600 °C in the fixed-bed reactor. In addition, the distributions
251 of oxygen and carbon elements show a gradual increase from the interior to the surface of the CaO
252 grains as shown in the EDX mapping of the FB-600 (Fig. 6f and g). By contrast, the weight percentage

253 of calcium exhibits a decrease from the inner grains to the surface of the FB-600 CaO. Similar results
254 are observed in Fig. 7c and d. The weight percentage of carbon on the surface of the commercial CaO
255 grains (5.96%) is twice as much as in the interior of the CaO grains (2.99%). This phenomenon
256 suggests that the carbonation reaction happened on the interface between CaO and CaCO₃. CO₂
257 diffuses through the CaCO₃ layer as CO₃²⁻ ions.⁴⁰ Therefore, the concentration of carbon elements
258 corresponding to CO₃²⁻ ions is higher on the surface of CaO grains after carbonation at 600 °C,
259 compared to the carbon concentration inside the CaO grains.

260 In this stage, CO₃²⁻ ions can decompose to produce CO₂ and O²⁻ as shown in Eq. (4). CO₂ molecule
261 transfers to a neighboring, similarly vacated site, while CO₂ produced elsewhere moves to take its
262 place and reform the CO₃²⁻. Therefore, the CO₂ molecule diffuses from site to site through the CaCO₃
263 product layer, until ultimately the carbonation reaction occurs at the interface between CaO and
264 CaCO₃. The ionic diffusion process is shown in Fig. S3b. A higher activation energy, about $179.2 \pm$
265 7.0 kJ mol^{-1} , is required for the decomposition of CO₃²⁻. This activation energy corresponds to a
266 carbonation temperature around 600 °C, where the second-stage fast CaO carbonation occurred.

267 The sudden change in activation energy between 500 and 600 °C could also be due to the phase
268 change of CaCO₃ from aragonite to calcite.⁴⁵ The diffusion of ions within aragonite is much easier
269 than calcite. The diffusion of ions (e.g., CO₃²⁻) is related to Tammann temperature (which is half the
270 absolute melting point, and the temperature at which bulk diffusion starts to become significant),
271 which is around 412 °C for aragonite and around 650 °C for calcite. In-situ XRD analysis of CaO
272 carbonation at a temperature of 750 °C has been investigated and, to date, only calcite was reported
273 ⁴⁶. However, at a lower carbonation temperature of 450 °C, aragonite-type CaCO₃ appears to be
274 formed, according to in-situ XRD experimental tests.⁴⁷

275 In this work, the phase changes in the carbonation reaction at different temperatures were investigated

276 using an in-situ XRD equipment, as shown in Fig. 8. It is found that calcite was the only phase of
277 CaCO_3 observed with the increase of both the reaction time and temperature. Therefore, the sudden
278 change of CaO carbonation is unlikely due to the phase change of CaCO_3 from aragonite to calcite
279 during the carbonation of CaO samples. However, a high-resolution synchrotron XRD could be used
280 to further confirm the absence of aragonite during CaO carbonation, which might exist as an
281 intermediate product.

282 In order to understand the influence of temperature on the critical thickness of the product layer during
283 the fast CaO carbonation, FIB-TEM coupled with selected-area electron diffraction patterns were
284 produced, as shown in Fig. 9. Even though no CaCO_3 product layer was observed in Fig. 9A, (012)
285 and (104) crystal phases of CaCO_3 were observed in the electron diffraction pattern (Fig. 9a) which
286 is in agreement with XRD results in Fig. 5a. In addition, (001) crystal phase ($\text{Ca}(\text{OH})_2$) was observed
287 due to the reaction between the thin FIB-TEM sample (around 100 nm) and moisture in the air. Three
288 distinct layers and single-crystal characteristics after the carbonation at 600 °C are shown in Fig. 9B
289 and Fig. 9b, respectively. The outside layer was caused by the coating of indium and platinum. The
290 compact layer in the middle was the formed CaCO_3 product layer, with a thickness around 90 nm.
291 This phenomenon indicates that, as with commercial CaO, carbonation at 400 °C and 600 °C involves
292 filling CaCO_3 in the small pores in the grains, and a product layer deposited on the outside of the
293 grains, respectively.

294 **3.4 Influence of porous structure**

295 Abundant mesopores, ranging from 2 to 100 nm, were generated by the lamellar structure in the sol-
296 gel CaO (Fig. 3b), which enhance the fast and kinetically-limited reaction stage. In addition, large
297 pore volume favors gas diffusion in the pore space of adsorbents.⁴⁸ Therefore, the sol-gel CaO
298 performed a higher carbon capture capacity compared to the commercial CaO in Table 2. No obvious

299 product layer was observed in the sol-gel CaO after carbonation at both 400 °C and 600 °C, as shown
300 in Fig. 6c and d. The distribution of carbon is consistent between the surface and the inner grains of
301 the sol-gel CaO grains (Fig. 7e and f). It appears that the carbonation of sol-gel CaO at 400 °C is
302 similar to that of commercial CaO, involving the filling of small pores in the CaO grains with the
303 formed CaCO₃. However, the carbonation at 600 °C is retarded by the lack of useful porosity (the
304 confinement effect) which is required for the growth of CaCO₃ instead of the formation of CaCO₃
305 product layer, as shown in Fig. 10b.⁴⁴ This is attributed to that local space is required for the growth
306 of particles from 16.7 to 36.9 cm³ mol⁻¹ for the conversion of CaO to CaCO₃. The FIB-TEM image
307 of sol-gel FB-600 as shown in Fig. 9C exhibits almost no porosity which is good agreement with the
308 FIB-SEM pictures in Fig. 6d. In addition, the crystal phases (CaCO₃ and Ca(OH)₂) were observed in
309 Fig. 9c, further indicating the formation of CaCO₃ in the sol-gel FB-600. Therefore, fabricating nano-
310 CaO having dimensions less than the critical thickness of the CaCO₃ layer (~90 nm) is of potentially
311 great significance if it can be done cheaply and in bulk. For example, nanowire and nanofilm of the
312 novel nano-CaO could be developed. However, the resistance of sorbent sintering during the process
313 of carbonation/calcination remains a challenging topic. Furthermore, it is suggested to disperse CaO
314 species into an inert support which can provide a certain extent of porosity, prohibit CaO sintering
315 and play an essential role in restricting the growth of CaCO₃ layer.

316

317 **4. Conclusions**

318 The formation of CaCO₃ product layer on the outside surface of CaO grains during the fast reaction
319 stage for carbon capture using two types of CaO has been systematically studied. It was found that
320 for both the commercial CaO and the sol-gel CaO, two distinct stages of fast carbonation are observed
321 at 400 and 600 °C. After carbonation at 600 °C for the commercial CaO, a layer of CaCO₃ with a

322 thickness around 90 nm is observed. This is because the internal pores of the commercial CaO grains
323 have been filled with CaCO₃ and a layer of the CaCO₃ product is deposited on the outside of the CaO
324 grain. Here, the fast carbonation stage of the commercial CaO is terminated by the formation of the
325 CaCO₃ layer. However, as with the synthesized sol-gel CaO, the carbonation reaction is retarded by
326 the lack of useful porosity (space is required for the formation of CaCO₃ due to its larger molar
327 volume than CaO), defined here as the confinement effect, instead of by the formation of a CaCO₃
328 product layer itself. Thus, a layer of CaCO₃ product on the sol-gel CaO cannot be observed after
329 carbonation at 600 °C. This is attributed to the presence of abundant mesopores generated by the
330 lamellar structure of the sol-gel CaO.

331

332 **Conflicts of interest**

333 There are no conflicts to declare.

334

335 **Acknowledgements**

336 The authors are grateful for the financial support of the National Natural Science Foundation of China
337 (no. 21706050) and China Scholarship Council (CSC, no. 201606450016).

338

339 **References**

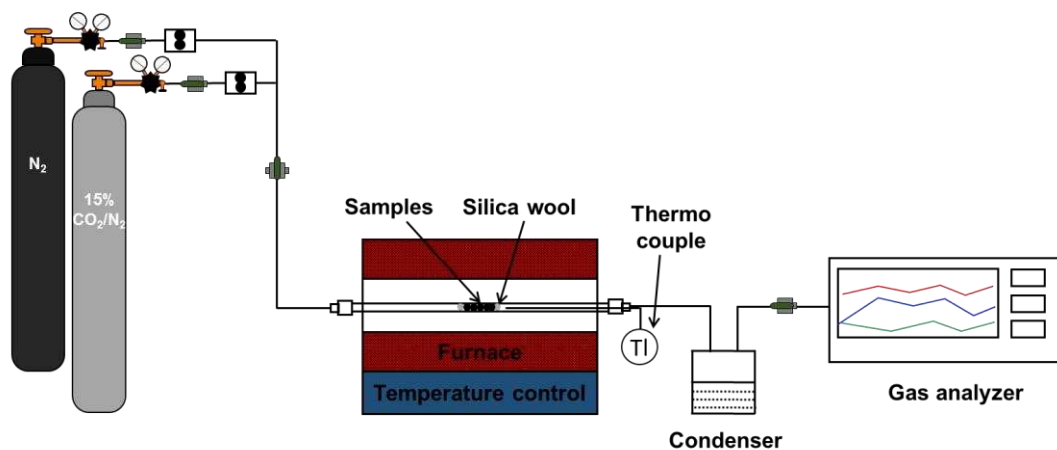
- 340 1. R. Han, J. Gao, S. Wei, Y. Su and Y. Qin, *J. Mater. Chem. A*, 2018, **6**, 3462-3470.
- 341 2. *Climate change 2014-impacts, adaptation and vulnerability: regional aspects*, Intergovernmental Panel on Climate
342 Change, 2014.
- 343 3. W. Obergassel, C. Arens, L. Hermwille, N. Kreibich, F. Mersmann, H. E. Ott and H. WangHelmreich, *Environmental*
344 *Law and Management*, 2016, **28**, 3-12.

- 345 4. F. Yan, J. Jiang, M. Zhao, S. Tian, K. Li and T. Li, *J. Mater. Chem. A*, 2015, **3**, 7966-7973.
- 346 5. H. Sun, J. Wang, J. Zhao, B. Shen, J. Shi, J. Huang and C. Wu, *Appl. Catal. B: Environ.*, 2019, **244**, 63-75.
- 347 6. R. S. Haszeldine, *Science*, 2009, **325**, 1647-1652.
- 348 7. M. M. Sadiq, H. Li, A. J. Hill, P. Falcaro, M. R. Hill and K. Suzuki, *Chem. Mater.*, 2016, **28**, 6219-6226.
- 349 8. Z. Sun, M. H. Sedghkerdar, J. Saayman, N. Mahinpey, N. Ellis, D. Zhao and S. Kaliaguine, *J. Mater. Chem. A*, 2014,
350 **2**, 16577-16588.
- 351 9. F. Wang and J. Chiou, *Energ. Convers. Manage.*, 2004, **45**, 15-26.
- 352 10. P. Zhao, J. Sun, Y. Li, K. Wang, Z. Yin, Z. Zhou and Z. Su, *Energy Fuels*, 2016, **30**, 7543-7550.
- 353 11. D. P. Hanak, E. J. Anthony and V. Manovic, *Energ. Environ. Sci.*, 2015, **8**, 2199-2249.
- 354 12. G. Melaet, W. T. Ralston, C. S. Li, S. Alayoglu, K. An, N. Musselwhite, B. Kalkan and G. A. Somorjai, *J. Am. Chem.*
355 *Soc.*, 2014, **136**, 2260-2263.
- 356 13. Y. A. Daza, R. A. Kent, M. M. Yung and J. N. Kuhn, *Ind. Eng. Chem. Res.*, 2014, **53**, 5828-5837.
- 357 14. H. Sun, C. M. Parlett, M. A. Isaacs, X. Liu, G. Adwek, J. Wang, B. Shen, J. Huang and C. Wu, *Fuel*, 2019, **235**, 1070-
358 1076.
- 359 15. J. Hilz, M. Helbig, M. Haaf, A. Daikeler, J. Ströhle and B. Epple, *Fuel*, 2017, **210**, 892-899.
- 360 16. B. Arias, M. Diego, J. Abanades, M. Lorenzo, L. Diaz, D. Martínez, J. Alvarez and A. Sánchez-Biezma, *Int. J. Greenh.*
361 *Gas Con.*, 2013, **18**, 237-245.
- 362 17. M. Chang, W. Chen, C. Huang, W. Liu, Y. Chou, W. Chang, W. Chen, J. Cheng, K. Huang and H. Hsu, *Energy*
363 *Procedia*, 2014, **63**, 2100-2108.
- 364 18. P. Sun, J. Grace, C. Lim and E. Anthony, *AIChE J.*, 2007, **53**, 2432-2442.
- 365 19. I. Yanase, T. Maeda and H. Kobayashi, *Chem. Eng. J.*, 2017, **327**, 548-554.
- 366 20. A. I. Lysikov, A. N. S. And and A. G. Okunev, *Ind. Eng. Chem. Res.*, 2007, **46**, 4633-4638.
- 367 21. S. Choi, J. H. Drese and C. W. Jones, *ChemSusChem*, 2009, **2**, 796-854.

- 368 22. R. Barker, *J. Appl. Chem. Biotech.*, 1973, **23**, 733-742.
- 369 23. H. Sun, C. Wu, B. Shen, X. Zhang, Y. Zhang and J. Huang, *Mater. Today Sustain.*, 2018, **1**, 1-27.
- 370 24. A. Kierzkowska, R. Pacciani and C. Müller, *ChemSusChem*, 2013, **6**, 1130-1148.
- 371 25. F. Campbell, A. Hills and A. Paulin, *Chem. Eng. Sci.*, 1970, **25**, 929-942.
- 372 26. B. Arias, J. Abanades and G. S. Grasa, *Chem. Eng. J.*, 2011, **167**, 255-261.
- 373 27. J. M. Valverde, *J. Mater. Chem. A*, 2013, **1**, 447-468.
- 374 28. F. Liu, W. Li, B. Liu and R. Li, *J. Mater. Chem. A*, 2013, **1**, 8037-8044.
- 375 29. D. Mess, A. F. Sarofim and J. P. Longwell, *Energy Fuels*, 1999, **13**, 999-1005.
- 376 30. D. Alvarez and J. C. Abanades, *Ind. Eng. Chem. Res.*, 2005, **44**, 5608-5615.
- 377 31. V. Nikulshina, M. E. Galvez and A. Steinfeld, *Chem. Eng. J.*, 2007, **129**, 75-83.
- 378 32. G. MontesHernandez, R. Chiriac, F. Toche and F. Renard, *Int. J. Greenh. Gas Con.*, 2012, **11**, 172-180.
- 379 33. H. Gupta and L. Fan, *Ind. Eng. Chem. Res.*, 2002, **41**, 4035-4042.
- 380 34. M. S. Duyar, M. A. A. Trevino and R. J. Farrauto, *Appl. Catal. B: Environ.*, 2015, **168**, 370-376.
- 381 35. E. Santos, C. Alfonsín, A. Chambel, A. Fernandes, A. S. Dias, C. Pinheiro and M. Ribeiro, *Fuel*, 2012, **94**, 624-628.
- 382 36. Y. Hu, W. Liu, J. Sun, X. Yang, Z. Zhou, Y. Zhang and M. Xu, *Energy Fuels*, 2016, **30**, 6606-6613.
- 383 37. B. C. Lippens and J. De Boer, *J. Catal.*, 1965, **4**, 319-323.
- 384 38. C. Luo, Y. Zheng, C. Zheng, J. Yin, C. Qin and B. Feng, *Int. J. Greenh. Gas Con.*, 2013, **12**, 193-199.
- 385 39. M. Broda, A. M. Kierzkowska and C. R. Müller, *ChemSusChem*, 2012, **5**, 411-418.
- 386 40. S. Bhatia and D. Perlmutter, *AIChE J*, 1983, **29**, 79-86.
- 387 41. H. Zhu, Z. Liu, Y. Wang, D. Kong, X. Yuan and Z. Xie, *Chem. Mater.*, 2007, **20**, 1134-1139.
- 388 42. C. Wu and P. T. Williams, *Appl. Catal. B: Environ.*, 2010, **96**, 198-207.
- 389 43. J. Dennis and R. Pacciani, *Chem. Eng. Sci.*, 2009, **64**, 2147-2157.
- 390 44. J. C. Abanades and D. Alvarez, *Energy Fuels*, 2003, **17**, 308-315.

- 391 45. A. Lucas, M. Mouallem-Bahout, C. Carel, J. Gaudé and M. Matecki, *J. Solid State Chem.*, 1999, **146**, 73-78.
- 392 46. W. Liu, J. S. Dennis, D. S. Sultan, S. A. Redfern and S. A. Scott, *Chem. Eng. Sci.*, 2012, **69**, 644-658.
- 393 47. A. Biasin, C. U. Segre, G. Salviulo, F. Zorzi and M. Strumendo, *Chem. Eng. Sci.*, 2015, **127**, 13-24.
- 394 48. Y. Kong, G. Jiang, M. Fan, X. Shen, S. Cui and A. G. Russell, *Chem. Commun.*, 2014, **50**, 12158-12161.
- 395
- 396

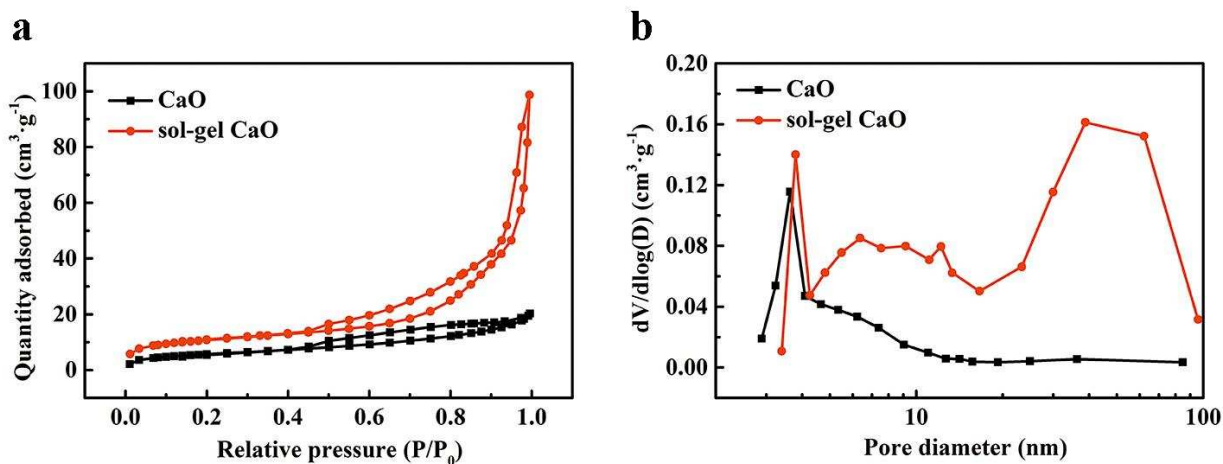
397



398

399 **Fig. 1** Schematic diagram of the atmospheric carbonation/calcination reactor system (fixed bed).

400



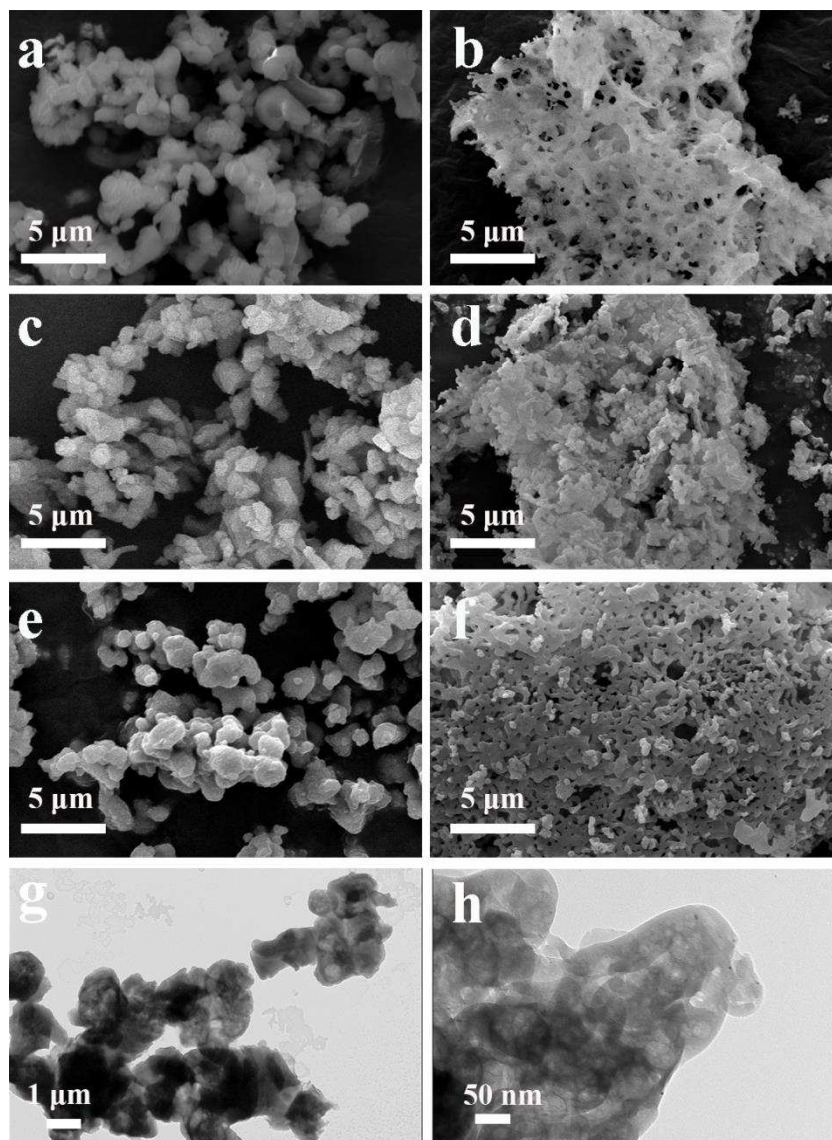
401

402 **Fig. 2** N₂ adsorption-desorption isotherms (a) and pore size distributions calculated from the BJH

403

desorption branch (b).

404

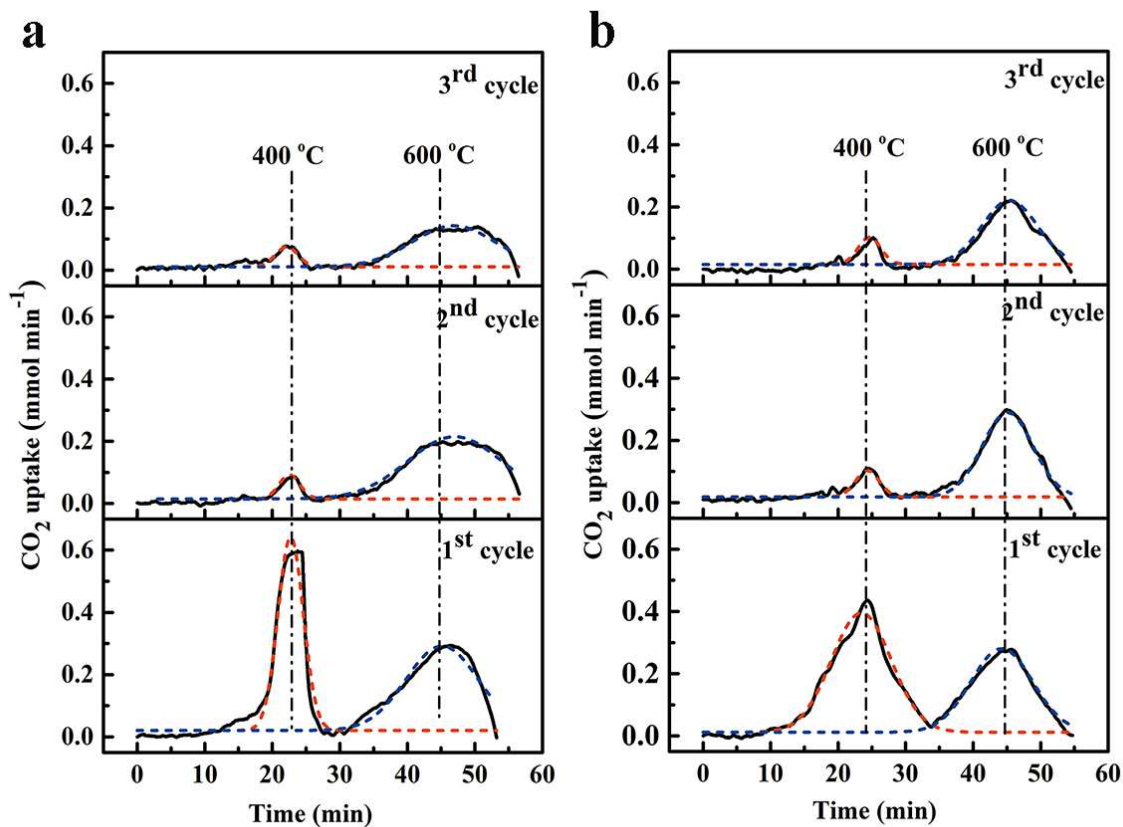


405

406

407

Fig. 3 SEM images of a) CaO, b) sol-gel CaO, c) FB-400, d) sol-gel FB-400, e) FB-600, f) sol-gel
FB-600 and TEM images of g) CaO, h) sol-gel CaO.

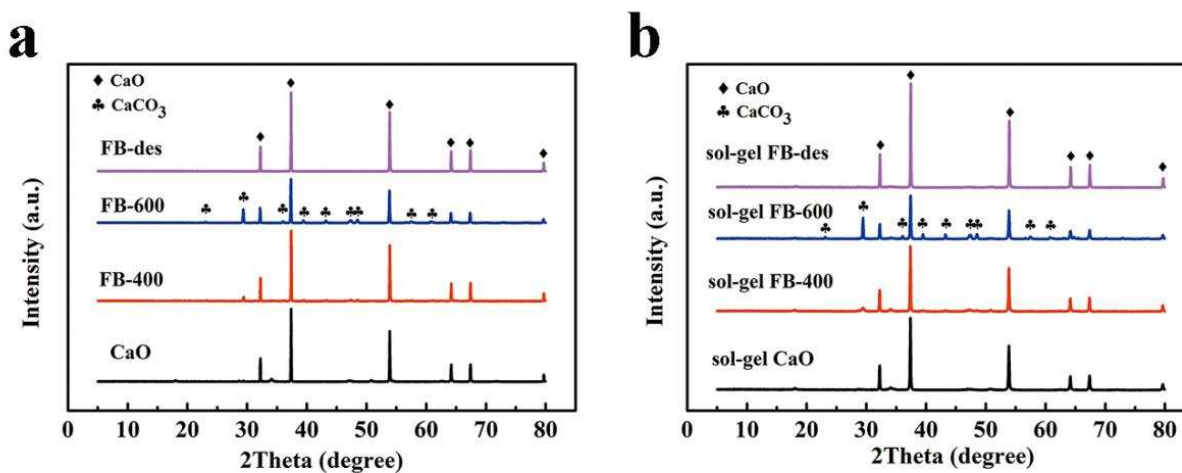


408

409 **Fig. 4** Cyclic CO₂ capture performance of a) CaO, b) sol-gel CaO, in a fixed-bed reactor (black line:

410 experimental curves; red dashed curve: peak I, carbonation at 400 °C, blue dashed curve: peak II,

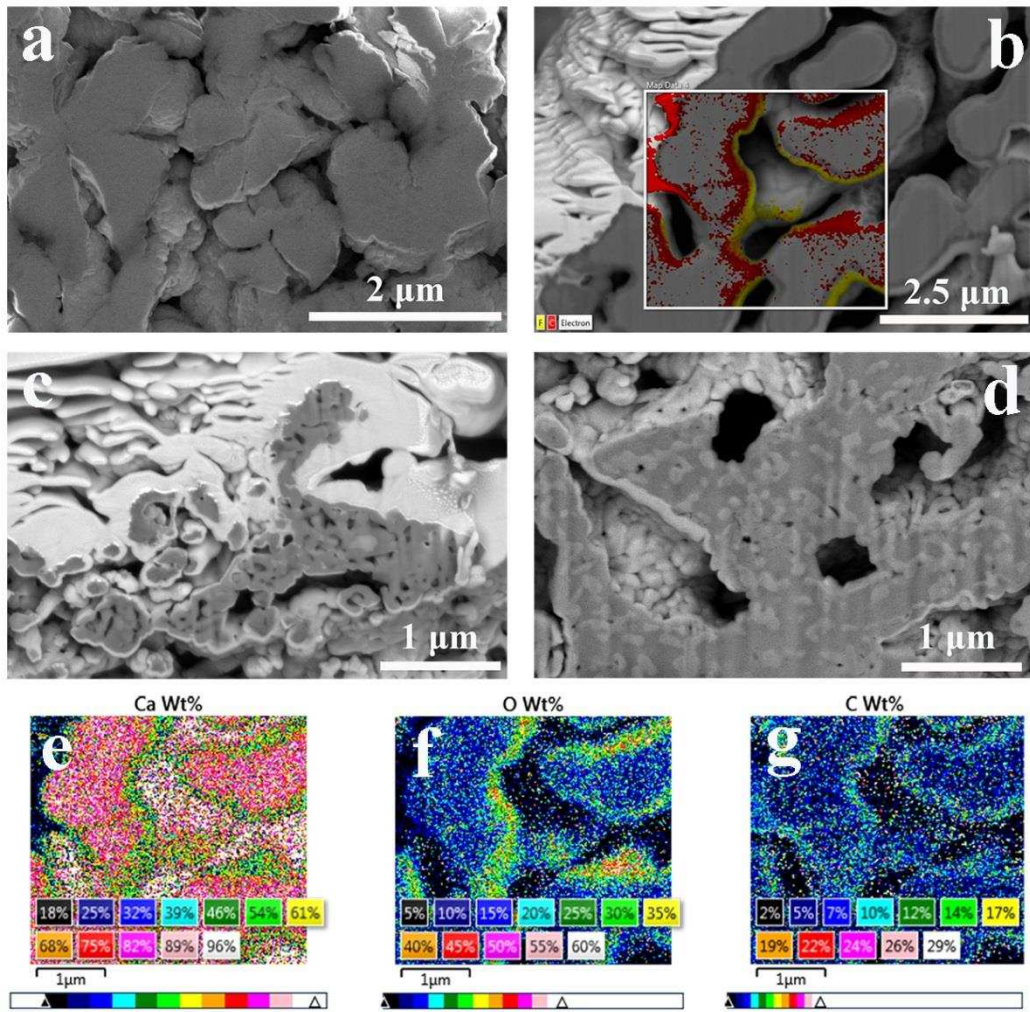
411 carbonation at 600 °C).



412

413 **Fig. 5** XRD patterns for CaO adsorbents obtained after reaching highest reaction rate at different

414 temperatures. a) CaO, b) sol-gel CaO.



415

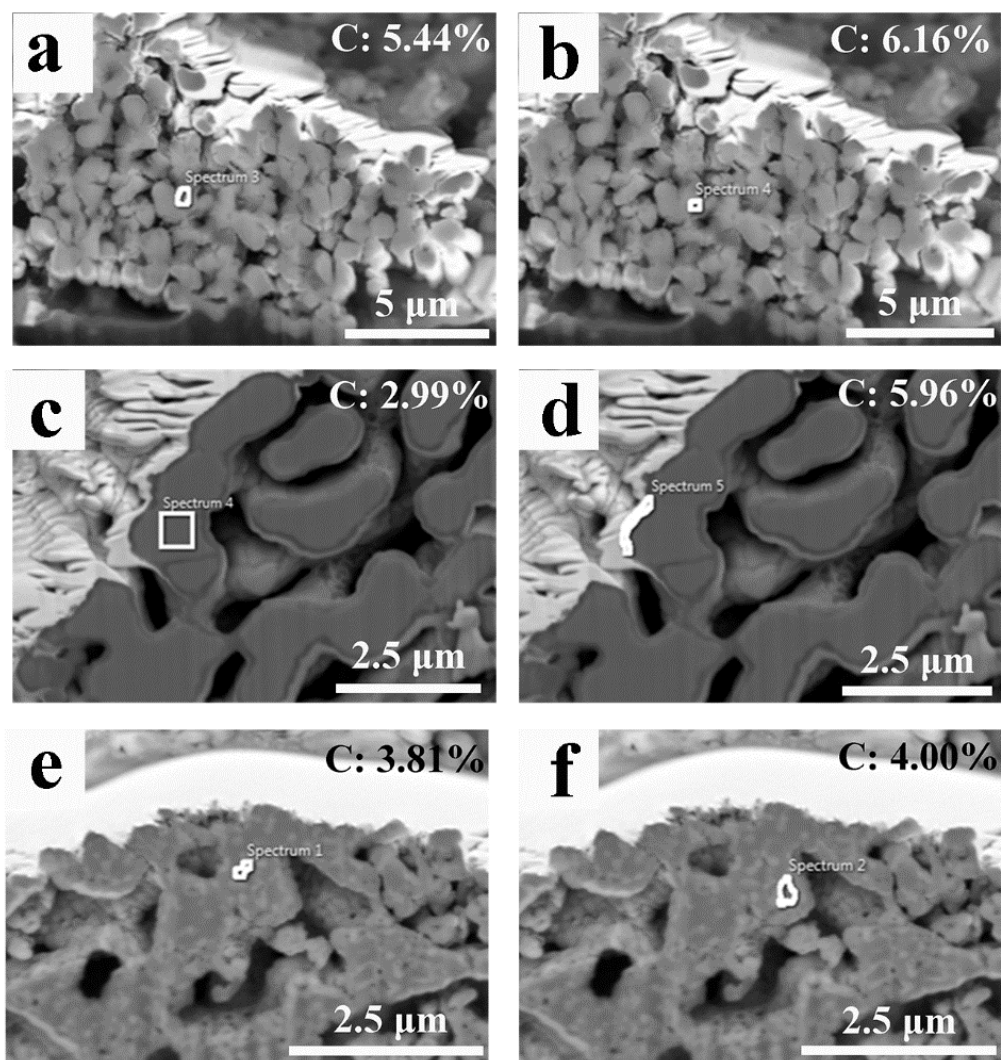
416 **Fig. 6** FIB-SEM images coupled with EDX mapping of the cross-section product layer. a) FB-400,

417 b) FB-600, c) sol-gel FB-400, d) sol-gel FB-600, e) Ca element mapping, f) O element mapping, g)

418

C element mapping.

419

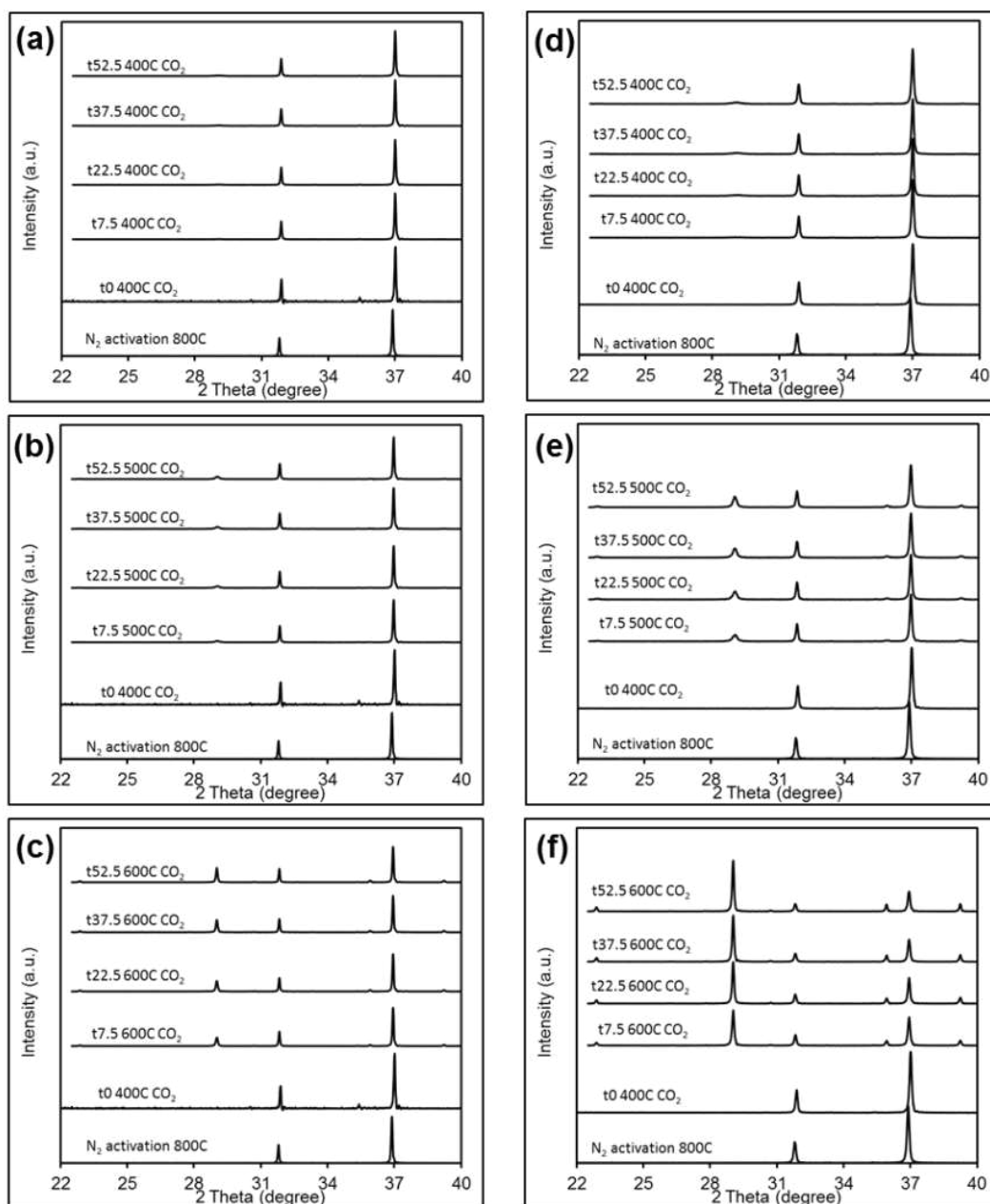


420

421 **Fig. 7** FIB-SEM images and carbon element percentage of a and b) FB-400, c and d) FB-600, and e

422

and f) sol-gel FB-600.



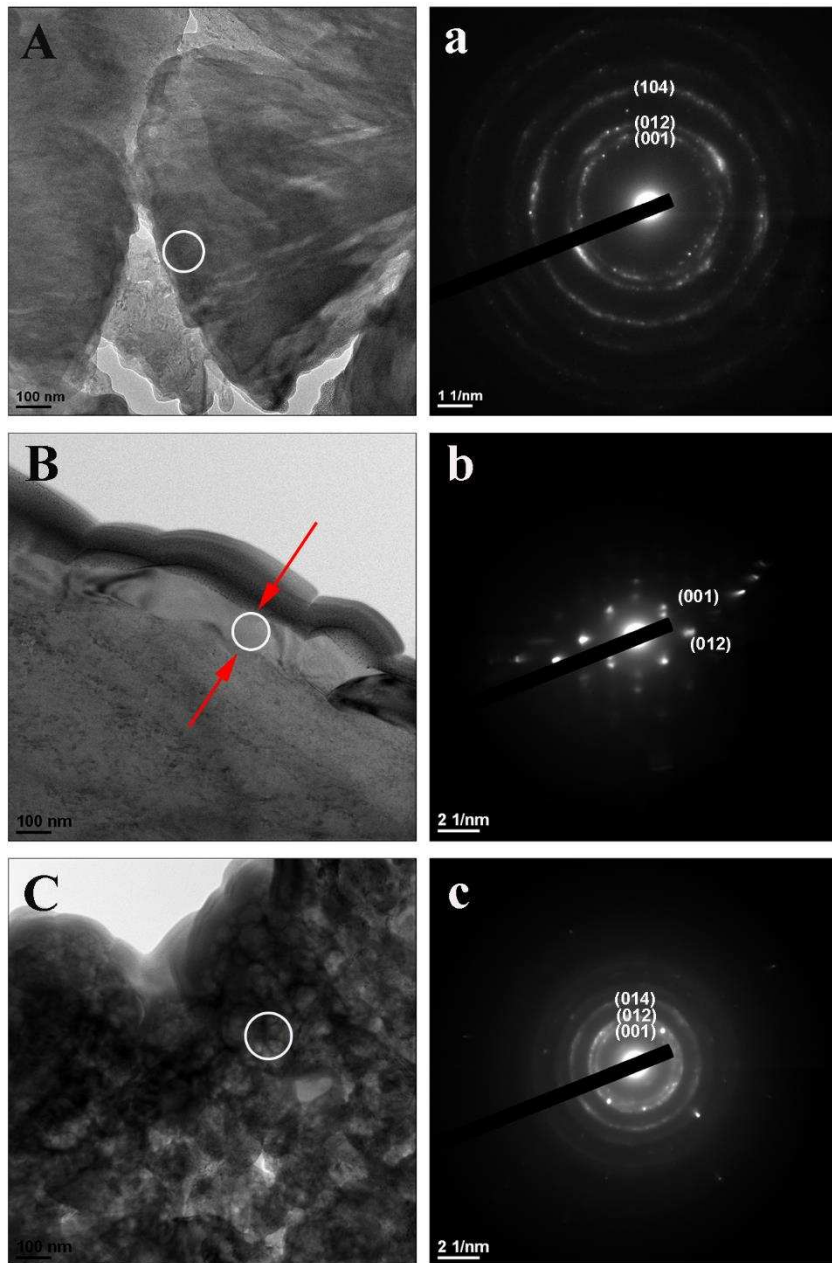
423

424 **Fig. 8** In-situ XRD patterns of CaO adsorbents at different temperatures. a) CaO 400 °C, b) CaO

425 500 °C, c) CaO 600 °C, d) sol-gel CaO 400 °C, e) sol-gel CaO 500 °C, f) sol-gel CaO 600 °C (txy.z

426

represents carbonation for xy.z min).

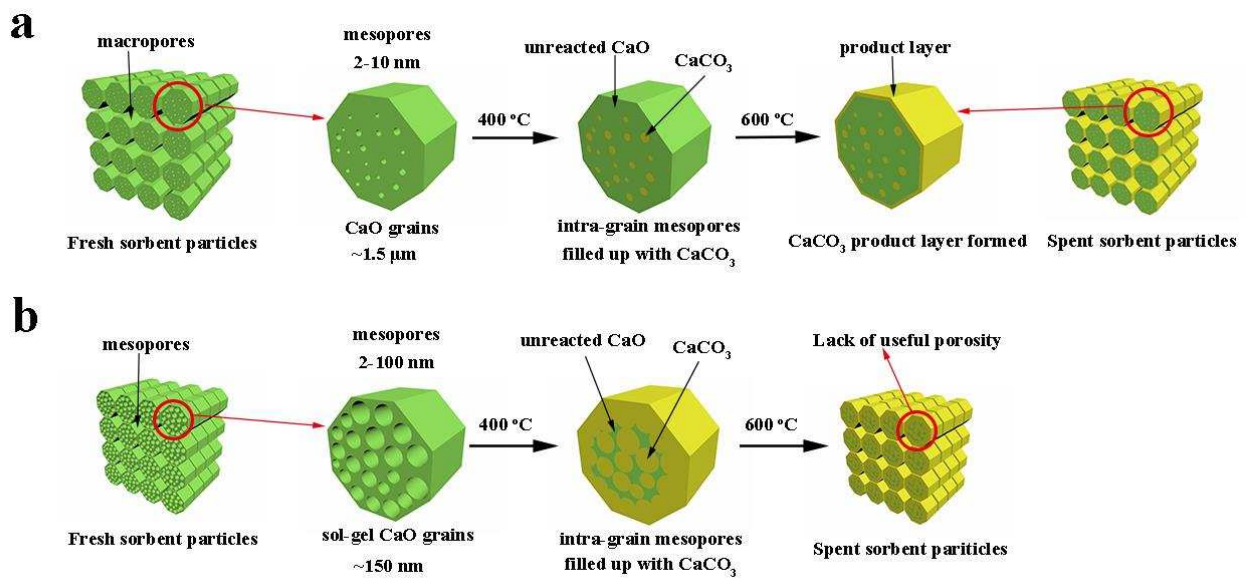


427

428 **Fig. 9** FIB-TEM images and selected-area electron diffraction pattern of the cross-section product

429

layer. A and a) FB-400, B and b) FB-600, C and c) sol-gel FB-600.



430

431

Fig. 10 Schematic illustration of the effect of temperature and structure on the CaCO₃ layer

432

thickness during CaO carbonation reaction. a) CaO, b) sol-gel CaO.

433

434

435

Table 1 Textural properties derived from different CaO adsorbents

Samples	$S_{\text{BET}}^{\text{a}}$	$S_{\text{micro}}^{\text{b}}$	$S_{\text{meso}}^{\text{c}}$	V_{p}^{d}	$V_{\text{micro}}^{\text{e}}$	$V_{\text{meso}}^{\text{f}}$
	($\text{m}^2 \text{g}^{-1}$)	($\text{m}^2 \text{g}^{-1}$)	($\text{m}^2 \text{g}^{-1}$)	($\text{cm}^3 \text{g}^{-1}$)	($\text{cm}^3 \text{g}^{-1}$)	($\text{cm}^3 \text{g}^{-1}$)
CaO	20.96	3.70	17.26	0.0314	0.0014	0.0331
sol-gel CaO	38.51	8.51	30.00	0.1527	0.0035	0.1511

436

^aBET surface areas

437

^bMicropore surface areas calculated by t-plot method

438

^cMesopore surface areas equal to S_{BET} minus S_{micro}

439

^dTotal pore volume measured at a relative pressure (P/P_0) of 0.99

440

^eThe t-plot micropore volume

441

^fBJH adsorption cumulative volume

442

Table 2 CO₂ uptake of a commercial CaO and a sol-gel CaO at different temperatures in a fixed-

444

bed reactor

CO ₂ uptake (mmol g^{-1})	1 st cycle		2 nd cycle		3 rd cycle	
	400 °C	600 °C	400 °C	600 °C	400 °C	600 °C
CaO	5.84	7.26	0.60	7.02	0.54	4.06
sol-gel CaO	8.50	6.16	0.76	5.12	0.74	4.20

445